

Research Article

Theoretical Investigation of the Structural, Spectroscopic, Electronic, and Pharmacological Properties of 4-Nerolidylcatechol, an Important Bioactive Molecule

Renyer A. Costa ¹, Earle Silva A. Junior,² Jaqueline de A. Bezerra,² Josiana Moreira Mar,¹ Emerson S. Lima ³, Maria Lucia B. Pinheiro,¹ Diego V. C. Mendonça,¹ Guilherme Braule P. Lopes,¹ Adjane Dalvana S. Branches,¹ and Kelson M. T. Oliveira¹

¹Department of Chemistry, Federal University of Amazonas (DQ-UFAM), 69077-000 Manaus, AM, Brazil

²Federal Institute of Science and Technology of Amazonas (IFAM), 69020-120 Manaus, AM, Brazil

³Faculty of Pharmaceutical Sciences, Federal University of Amazonas, 69077-000 Manaus, AM, Brazil

Correspondence should be addressed to Renyer A. Costa; renyer.costa@gmail.com

Received 30 June 2018; Accepted 18 November 2018; Published 13 January 2019

Academic Editor: Franck Rabilloud

Copyright © 2019 Renyer A. Costa et al. This is an open access article distributed under the Creative Commons Attribution License, which permits unrestricted use, distribution, and reproduction in any medium, provided the original work is properly cited.

4-Nerolidylcatechol (4NRC), a secondary metabolite described as a potent antioxidant that presents anti-inflammatory, antimalarial, analgesic, and cytotoxic properties, has been receiving prominence in the catechol class. In this work, a theoretical DFT study of the vibrational, structural, and quantum properties of 4-nerolidylcatechol (4NRC) using the B3LYP/6-311G (2d,p) level is presented. The theoretical molecular geometry data were compared with the X-ray data of a similar molecule in the associated literature and a conformational study is presented, with the aim of providing a good comprehension of the 4NRC structural arrangement and stability. Also, HOMO-LUMO energy gap and natural bond orbitals (NBOs) were performed and discussed. The calculated UV spectrum showed similarity to the experimentally obtained data, with transitions assigned. The comparative IR studies revealed that intermolecular hydrogen bonds that stabilize dimeric forms are plausible and also allowed the assignment of several characteristic vibrations. Molecular docking calculations with DNA topoisomerase I-DNA complex (TOPO-I), glyceraldehyde 3-phosphate dehydrogenase (GAPDH), and *Plasmodium falciparum* lactate dehydrogenase (PfLDH) showed binding free energies of -6.3 , -6.5 , and -7.6 kcal/mol, respectively, which indicates that 4NRC is a good competitive inhibitor for these enzymes.

1. Introduction

Catechols are a group of small molecules with physiological importance, acting as effective structural units in many adrenergic, Parkinson's disease [1], attention-deficit hyperactivity disorder (ADHD) [2], bronchodilator, antidepressants, antihypertensive drugs, perfumes, and agrochemical ingredients (for the production of pesticides) [3]. In organic chemistry, catechol (1,2-dihydroxybenzene) and its derivatives have widely attracted scientists since decades principally for the design of mussel-inspired synthetic adhesives and coatings [4]. With respect to their biological importance, catechols can occur as metabolites [5, 6] or as endogenous compounds, such as neurotransmitter and their precursors as adrenaline, noradrenaline, dopamine, and L-DOPA [1, 5, 6].

Catechols could act as antioxidants, preventing lipid peroxidation, and as pro-oxidant-damaging macromolecules such as DNA [7].

An important representative of this class of molecules is 4-nerolidylcatechol (4NRC) (Figure 1). Its potent antioxidant activity is largely established in the literature [8–12], but other pharmacological properties, such as antimicrobial [13], analgesic, anti-inflammatory [14], cytotoxic [15, 16], and antimalarial activities [17] are related to 4NRC. It is the major secondary metabolite of *Piper* genus plants, traditionally known for their use in the treatment of various diseases [12, 15, 17–20]. However, the therapeutic applicability of 4NRC is limited by its very poor water solubility.

Many works in the literature have discussed the pharmacological properties [10, 12, 16, 18–22] of 4NRC, but

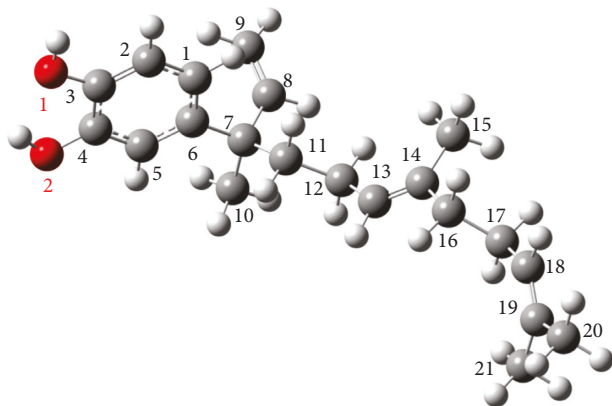


FIGURE 1: Optimized structure of the most stable conformation in the gas phase of 4-nerolidylcatechol (4NRC) with scheme of atom numbering.

studies on the chemical-quantum, spectroscopic, and structural properties of 4NRC are still lacking. This work discusses 4NRC, isolated from *Piper peltatum* L., through a theoretical DFT approach (geometry, HOMO-LUMO orbitals, natural bond orbitals, and conformational analysis) based on experimental data (X-ray, UV, and FTIR), providing a more detailed description of the 4NRC structure and properties. Docking calculations were also performed with the objective of evaluating the interaction of this molecule with enzymes that justify its antimalarial and cytotoxic potential. As far as we know, no theoretical molecular modeling study that discusses the spectroscopic behavior of 4NRC with the quantum chemical DFT approach has been presented. It is important to mention that theoretical quantum models, such as DFT, and advanced software constitute a powerful tool for the study of the properties of several compounds and ultimately for the study of properties of secondary metabolites of plants [23–26]. However, it is important to mention that a theoretical study of the interaction of 4NRC with 2-hydroxypropyl- β -cyclodextrin (HP- β -CD) was performed previously but through a mechanical molecular approach [27].

2. Methodologies

4-Nerolidylcatechol was isolated of inflorescences from *P. peltatum* L. collected in March 2017 at the Federal University of Amazonas Campus, northern sector, Manaus City, Amazonas, Brazil (SISBIO n. 55863-1). The sample was dried, ground, and subjected to successive extraction in an ultrasonic bath, obtaining hexane and ethyl acetate extracts. A portion of the ethyl acetate extract was subjected to Sephadex LH20 column with hexane, dichloromethane, and methanol (2:5:1). After TLC analysis, part of catechol-rich fraction was submitted to preparative TLC plate and eluted with hexane and ethyl acetate (7:3, two times) for isolation of 4NRC. The substance was confirmed by comparison with a 4NRC sample previously isolated by our group. The substance shows oil aspect and was solubilized with chloroform and then mixed with KBr salt until the solvent was evaporated for obtention of the FT-IR spectrum. The pastille was analyzed by a Thermo Scientific Nicolet iS10 infrared spectrometer in the spectral region from 4000 to 400 cm^{-1} . The sample was solubilized with ethanol and

analyzed by an ultraviolet visible spectrometer (Global Trade, UV-5100) in the range between 190 and 300 nm. The quantum-chemical calculations were performed on the Gaussian 09 D.01 Program [28] on Debian LINUX (8.0 version) platform using an INTEL Quadcore™ PC 16 GB. The DFT approach was selected for the calculations using the 6-311G (2d,p) basis sets and the B3LYP functional. To evaluate conformers' stability and energy barriers, scan calculations have been performed which consisted in 30 steps varying by 12° (totalizing a 360° turn) the dihedral angles C11-C12-C13-C14, C13-C14-C16-C17, and C16-C17-C18-C19. The most stable conformations (potential energy wells) were resubmitted to the same scan calculations procedure in order to find the structures with the lowest potential energy (minima geometry). All the minima structures were optimized by the force gradient method using Berny's algorithm and a standard analytical harmonic vibrational analysis (no imaginary frequencies or negative eigenvalues were found). The obtained theoretical IR spectra from the calculated DFT vibrational wavenumbers were uniformly scaled by a factor of 0.98. The UV spectra were calculated using the time-dependent density functional theory (TD-DFT) with B3LYP/6-311G (2d,p) and 6-311G++ (2d,p) basis set in methanol (polarizable continuum model). NBO values were obtained with the program NBO 3.1, implemented in the GAUSSIAN 09 package. The assignments of the calculated IR wavenumbers were aided by the animation option present in GAUSSVIEW 5.0, which promotes a visual presentation of the vibrational modes [29]. The potential energy distribution (PED) was calculated using the VEDA 4 software package [30]. The basis set superposition error (BSSE) of the interaction energies of the dimer was corrected by the counterpoise (CP) method [31]. The methodology consisted in the single point (a posteriori) CP corrections on the conventionally optimized structures (which are not minima on the CP-corrected surfaces).

3. Results and Discussions

3.1. Geometry Optimization and Conformational Analysis.

The theoretical geometry optimization results of the studied molecules, which were calculated using the B3LYP/6-311G (2d,p) approach, were compared with X-ray data for epinine

hydrobromide [32], due to the fact that it is a similar structure (Table S1). The compound shows certain polarities being soluble in chloroform and ethyl acetate, with a theoretical dipole moment of 2.09 D. The structure showed stable conformations and good structural cohesion with C1 symmetry and energy values of -968.97 a.u. Concerning its bond length, the benzene ring presents uniformity revealing values around 1.39 Å. The side chain attached to the ring presents slightly distortions with bond values of 1.54 Å (C6-C7), 1.56 Å (C7-C11), 1.54 Å (C11-C12), 1.50 Å (C12-C13), 1.33 Å (C13-C14), 1.51 Å (C14-C16), 1.54 Å (C16-C17), 1.50 Å (C17-C18), and 1.33 Å (C18-C19). Relative to the angles, the structure reveals slight distortions, including the benzene ring, that showed the values of 121.33° (C2-C1-C6), 117.56° (C1-C6-C5), 121.57° (C6-C5-C4), and 119.84° (C5-C4-C3) (Table S1).

The potential energy surfaces (PES) analysis revealed a total of six stable conformational isomers (besides the initial conformer A) that correspond to the minima energies resulting from the performed scans (Figure 2). Initially, conformer A was submitted to three PES calculations, involving the dihedral angles C11-C12-C13-C14, C13-C14-C16-C17, and C16-C17-C18-C19, which revealed conformers B, C, and D, respectively, as minima geometries. Each obtained conformer was resubmitted to two PES calculations involving the following dihedral angles: C13-C14-C16-C17 and C16-C17-C18 for conformer B, resulting in conformations B1 and B2, respectively, as minima energies; C11-C12-C13-C14 and C16-C17-C18 for conformer C, resulting in conformations C1 and C2, respectively, as minima geometries; C11-C12-C13-C14 and C13-C14-C16-C17 for conformation D presenting conformations D1 and D2, respectively, located at the energy wells. An accurate analysis of spatial arrangement of the conformers showed that structures B1 and D1, B2 and C1, C2 and D2 are the same, resulting in a total of seven structures rather than ten, evidencing that such conformers are obtained through different rotational routes. Concerning the total energy values, conformer B showed the lowest (-968.9768142 a.u.) setting the most stable structure followed by conformers A (-968.9767925 a.u.), C2(D2) (-968.9767353 a.u.), D (-968.9766598 a.u.), C (-968.9766418 a.u.), B1(D1) (-968.9766112 a.u.), and B2(C1) (-968.9765563 a.u.) (Figure 3). Despite the close values between the conformations, it is important to note that there will be an energetic barrier to overcome, as seen in Figure 2, and rotations involving the C14-C16 bond axis showed the highest energy barrier values (~ 4 kcal/mol) while rotations involving the C12-C13 and C17-C18 bond axis presented lowest energy barrier values (0.9 kcal/mol and 1.1 kcal/mol, respectively). Based on the values of total energy, all the following calculations were performed using conformation B (lowest energy conformation); however, due to the small values of ΔE (and small energy barrier values), it is not ruled out that the other conformations, showed in Figure 3, exist in the reactive medium.

3.2. HOMO and LUMO Analysis. The molecular orbital (MO) is a very important concept in quantum chemistry,

being extensively employed to describe the chemical behavior. The highest occupied molecular orbital (HOMO) and lower unoccupied molecular orbital (LUMO) are the two most important molecular orbitals in a molecule as both are used to describe various chemical properties such as reactivity and kinetics [33–35]. Also, these orbitals are an indispensable tool for the description of other phenomena involving molecular electronic structures, such as charge transfer, photoexcitation, and molecular electronics. According to the Janak theorem [36] and Perdew et al. [37] MO theory approaches, the HOMO energy (ϵ_{HOMO}) is related to the IP, and the LUMO energy (ϵ_{LUMO}) has been used to estimate the electron affinity (EA), making it possible to calculate the important reactivity indices hardness (η), chemical potential (μ), electronegativity (χ), and electrophilicity index (ω) which are defined as follows [36–38]:

$$\begin{aligned}\eta &= \frac{1}{2} \left(\frac{\partial \mu}{\partial N} \right)_V = \frac{1}{2} \left(\frac{\partial^2 E}{\partial N^2} \right) = \frac{(I + A)}{2}, \\ -\mu &= \chi = - \left(\frac{\partial E}{\partial N} \right)_V = \frac{(I + A)}{2}, \\ \omega &= \left(\frac{\mu^2}{2\eta} \right).\end{aligned}\quad (1)$$

The hardness (η), defined as the second derivative of the total energy, together with the concept of electronegativity and the principle of equalization of electronegativities, has been used to develop the principle of hard and soft acids and bases. Electrophilicity index (ω) [39, 40] is the measure of the extent of the electrophilicity of a molecule. The chemical potential (μ) provides a global reactivity index, being interpreted as a charge transfer from a system of higher chemical potential to the one of lower chemical potential. Electronegativity (χ) represents the power to attract electrons and is equal to the negative of the chemical potential. All these properties were calculated for 4NRC at B3LYP/6-311G (2d,p) basis set using the above equations, and their values are shown in Table 1. As seen in Figure 4, the calculated HOMO and LUMO for 4NRC are located in the aromatic moiety (catechol moiety), indicating that this region is more susceptible to accepting or donating electrons, implying that the catechol moiety is the portion of higher reactivity and activity of the molecule. The HOMO-LUMO gap energy value (5.67 eV) indicates a good reactivity of 4NRC. The small hardness (η) value (2.83 eV) shows its high polarizability, leading to infer that 4NRC presents soft molecule behavior, with the electrons further from the nucleus (in the case of the phenolic moiety). The electronegativity (χ) and electrophilicity index (ω) values reveals that 4NRC has good attractive electron power and acts as a moderate electrophile.

3.3. UV-Vis Analysis. The electronic spectrum of 4NRC in ethanol was compared to the calculated spectrum at time-dependent density functional using B3LYP/6-311 G (2d,p) and B3LYP/6-311++G (2d,p) basis set in ethanol by the PCM model as shown in Figure 5. The experimental spectrum of

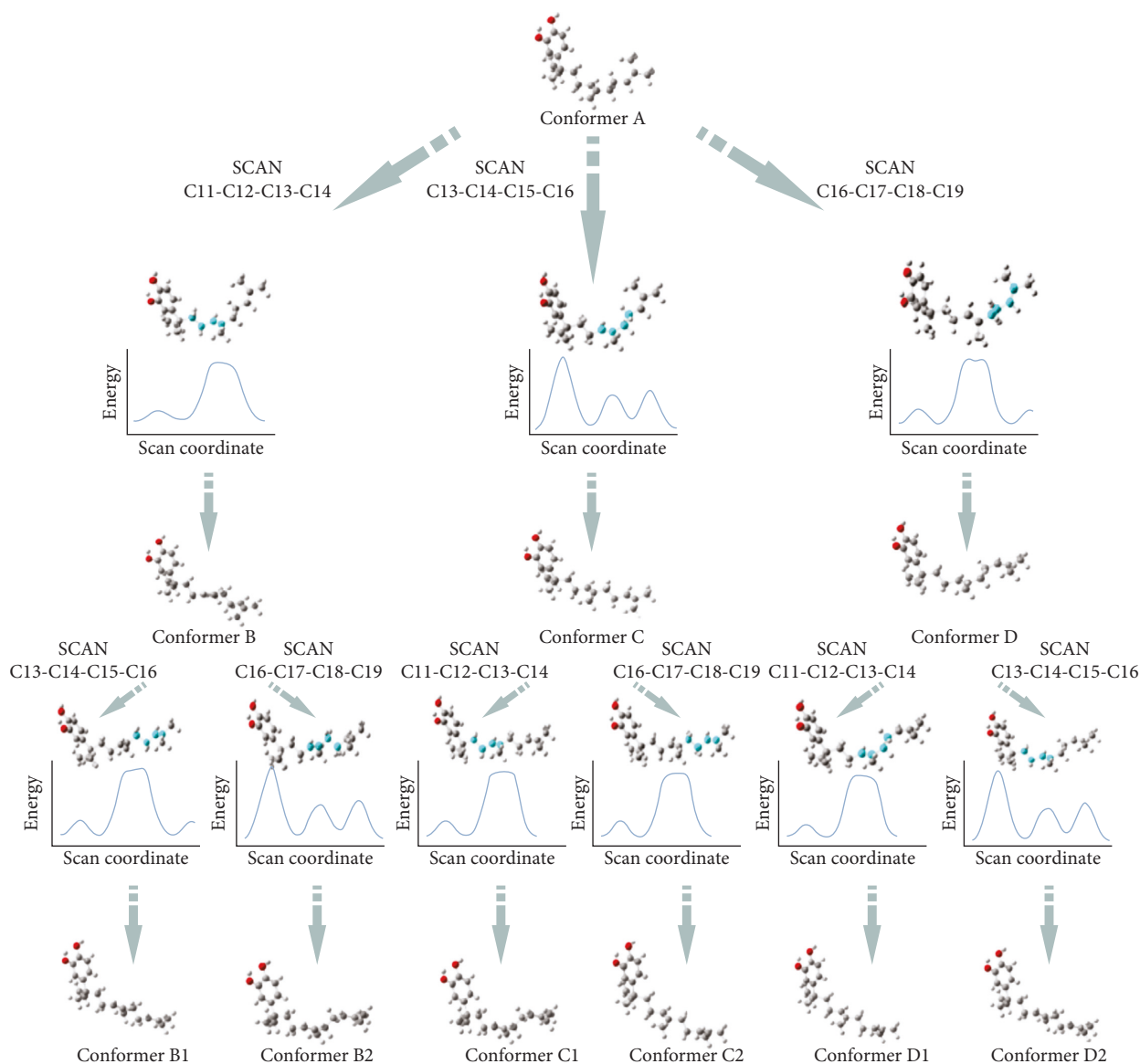


FIGURE 2: Scheme for potential energy surfaces (PES) analysis of 4NRC.

the structure presented bands at 200 and 280 nm that were assigned to the sum of the $\sigma \rightarrow \pi^*$ and $\pi \rightarrow \pi^*$ transitions characteristic of catechols with conjugated system [22]. The theoretical spectrum calculated at B3LYP/6-311++G (2d,p) presented an intense electronic transition of 6.03 eV at 205.46 nm (oscillator strength $f = 0.2438$) with major contributions from $H - 3 \rightarrow L$ (24.8%), $H - 3 \rightarrow L + 3$ (13.7%), and $H - 3 \rightarrow L + 2$ (12.23%), being equivalent to the experimental band at 200 nm. The calculation also predicted intense electronic transition at 257.51 nm (4.81 eV) that are equivalent to the experimental bands at 280 nm, corresponding to the contribution of the electronic transition from $H \rightarrow L$ (83.46%). In B3LYP/6-311 (2d,p) calculation, the theoretical spectrum presented an intense electronic transition of 6.07 eV at 204.31 nm (oscillator strength $f = 0.2505$), with major contributions from $H \rightarrow L + 2$ (82.57%) and a transition of 4.90 eV at 252.87 nm (oscillator strength $f = 0.1357$) with major contributions

from $H \rightarrow L$ (82.88%). Concerning the employed basis set, B3LYP 6-311++G (2d,p) presented a better performance; however, B3LYP 6-311 G (2d,p) showed close values to the experimental ones too, revealing a good applicability of this base for the prediction of absorption spectra.

3.4. IR Analysis. The assignment of the experimental bands to the vibration modes was made using the lowest energy structure, conformation B, by the calculated potential energy distribution (PED). A total of 153 normal vibration modes were obtained; however, only the modes between 400 and 4000 cm^{-1} were compared with the experimental IR data (Table 2). Figure 6 shows the superimposition of the experimental and theoretical IV spectra of 4NRC. The bands between 3200 and 2500 cm^{-1} were assigned to OH (band at 3468 cm^{-1}), aromatic C-H (band at 2968 cm^{-1}), and CH_2 stretching modes (bands at 2932 and 2923 cm^{-1}). Bands

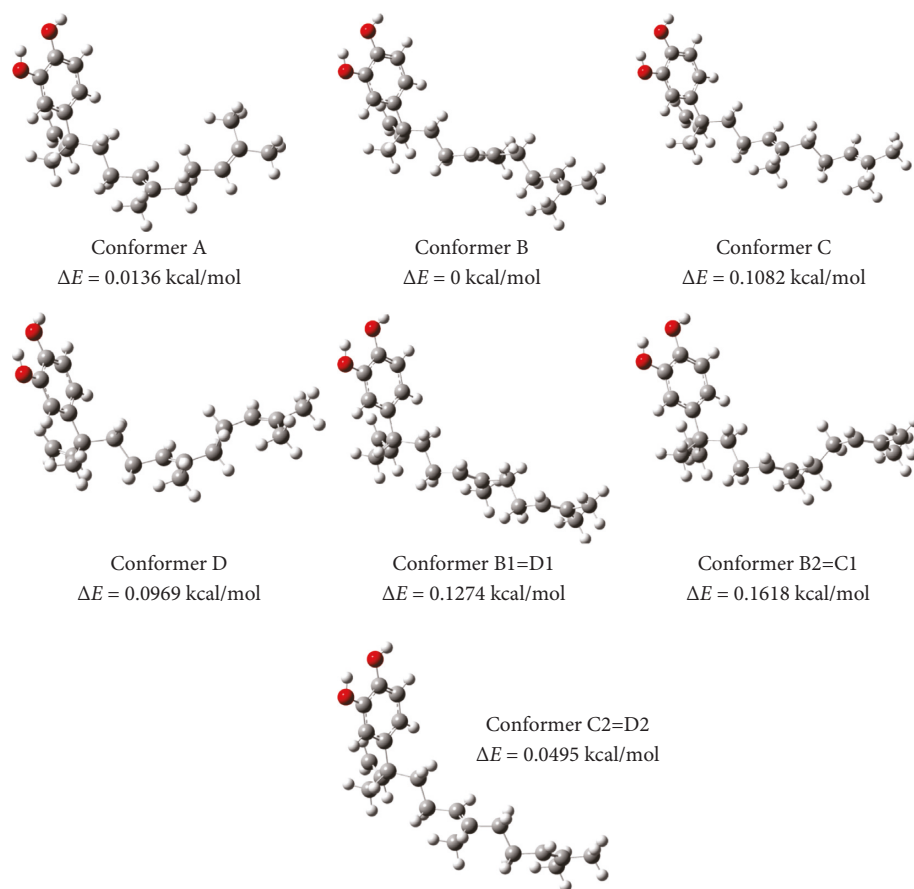


FIGURE 3: Stable conformational isomers of 4NRC.

TABLE 1: Calculated energy parameters for 4NRC using B3LYP/6-311 G (2d,p) basis set.

Parameters	4-Nerolidylcathecol
Energy (a.u.)	-968.9768
Dipole moment (debye)	2.09
E_{HOMO} (eV)	-5.68
E_{LUMO} (eV)	-0.01
$E_{\text{HOMO-LUMO}}$ (eV)	5.67
$E_{\text{HOMO-1}}$ (eV)	-6.19
$E_{\text{LUMO+1}}$ (eV)	-0.18
$E_{(\text{HOMO-1})-(\text{LUMO+1})}$ (eV)	6.01
Hardness (η)	2.83
Chemical potential (μ)	-2.84
Electronegativity (χ)	2.84
Electrophilicity index (ω)	1.42

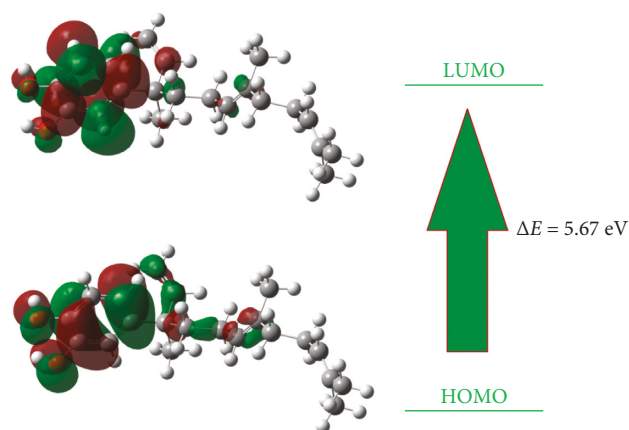


FIGURE 4: Frontier molecular orbitals of 4NRC.

between 1700 and 1000 cm^{-1} were assigned to $\text{C}=\text{C}$ stretching vibrations (bands at 1636 , 1520 , and 1283 cm^{-1} correspond to calculated theoretical scaled wavenumbers 1628 , 1519 , and 1278 cm^{-1} , respectively), $\text{C}-\text{C}$ stretching vibrations (bands at 1114 , 1082 , and 1001 cm^{-1} correspond to calculated theoretical wavenumbers 1108 , 1080 , and 1000 cm^{-1} , respectively), $\text{H}-\text{C}=\text{C}$ and $\text{H}-\text{C}-\text{H}$ bend vibration modes (bands at 1440 , 1383 , and 1283 cm^{-1} correspond to the theoretical scaled wavenumbers 1444 , 1395 , and 1278 cm^{-1} , respectively). Bands between 980 and 400 cm^{-1}

are mainly related to HCCC torsions, $\text{C}-\text{C}$ stretching vibrations, and OCCC/CCCC out of plane vibration modes. The large differences in the 3500 to 4000 cm^{-1} region (related to the O-H stretching) between the theoretical and experimental spectra are indicative that interactions among 4NRC molecules occur, in this case, intermolecular interactions involving the O-H group. The proposed 4NRC dimer (Figure 7) showed stabilization due to the existence of an intermolecular hydrogen bond of O-H-O type. The theoretical wavenumber assigned to the O-H group stretching

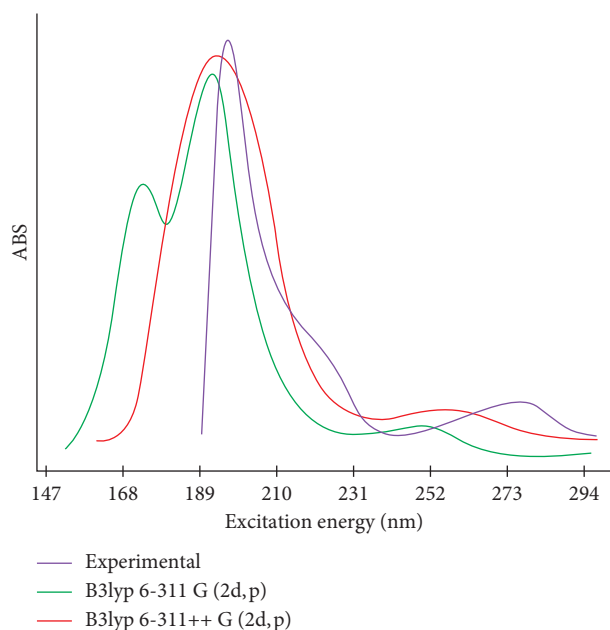


FIGURE 5: Comparison between experimental and theoretical UV spectra of 4NRC at B3LYP 6-311G (2d,p) and B3LYP 6-311G++ (2d,p) in ethanol.

in the dimer, 3595.62 cm^{-1} , is closer to the experimental ones, 3468 cm^{-1} , while the monomer showed discrepant wavenumber values, 3767.29 and 3712.40 cm^{-1} . Regarding the stability of the proposed dimer, the analysis was given through ΔE (interaction energy value), defined as follows:

$$\Delta E = E_{\text{dimer}} - 2E_{\text{monomer}}, \quad (2)$$

where the interaction energy ΔE is -8.26 kcal/mol , which reveals that the dimer is more stable in relation to the separated monomers. Applying the counterpoise correction, the corrected ΔE value is -4.58 kcal/mol . It is important to note that each monomeric unit of the proposed dimer presents slight distortions in the geometry compared to the most stable calculated conformer (conformer B), which makes the value of ΔE questionable, as slight changes in the geometry imply differences in the energy value. The counterpoise correction methodology considers only the energies of the monomers that constitute the dimer, but does not consider the fact that the monomers can change their geometry when they form a dimer. In view of this, other ΔE calculation can be taken into account in this case, considering the energy of monomer B and the corrected energy of the CP dimer (counterpoise corrected energy):

$$\Delta E = E_{\text{CP dimer}} - 2E_{\text{monomer B}}, \quad (3)$$

which results in a corrected ΔE of -3.51 kcal/mol and an incorrect ΔE of -7.15 kcal/mol .

3.5. NBO Study. Natural bonding orbitals (NBOs) are localized orbitals of few centers (typically 1 or 2) and of maximum occupancy that are composed of natural hybrid orbitals (NHOs) from the optimized linear combination of

NAOs of a given set of atoms. The NBO analysis provides very important information, especially for organic chemists, of a molecule because it presents a localized representation of the natural Lewis structure (NLS) of the wave function, such as delocalisation degree of the electron structure, orbital interactions charge balance, and binding order. The orbital interactions (hyperconjugation interactions), which constitute a notorious stabilizing factor of a molecule, are given by the second-order perturbation energies $E(2)$ [donor (i) \rightarrow acceptor (j)] in the NBOs calculations, which is defined as follows [41–43]:

$$E(2) = \Delta_{ij} = q_i \frac{F_{ij}^2}{\epsilon_j - \epsilon_i}. \quad (4)$$

Thus, NBOs constitute an important theoretical tool for analysis, because they provide a description of valence bond type of the wave function closely linked to the classical concepts of Lewis structure, which makes the NBOs useful in understanding the delocalisation of the electron density [44–47]. The NBO analysis (Table S2) for the title molecule revealed strong hyperconjugative intramolecular interactions of $\pi \rightarrow \pi^*$, $\sigma \rightarrow \pi^*$, and $\text{LP} \rightarrow \pi^*$ transitions that lead to an intramolecular electronic density transfer, causing stabilization of the molecular system in 4NRC. The second-order perturbation energy analysis shows greater conjugations in the benzene ring principally by $\pi \rightarrow \pi^*$ and $\text{LP} \rightarrow \pi^*$ interactions as C5-C5 \rightarrow C1-C2 (19.46 kcal/mol), C1-C2 \rightarrow C3-C4 (20.03 kcal/mol), C3-C4 \rightarrow C5-C6 (18.77 kcal/mol), C3-C4 \rightarrow C1-C3 (21.53 kcal/mol), O1 \rightarrow C3-C4 (21.98 kcal/mol), and O2 \rightarrow C3-C4 (21.98 kcal/mol). $\sigma \rightarrow \sigma^*$ hyperconjugative intramolecular interactions also occur and contributes to the stabilization of the system deserving prominence in the interactions C13-H13 \rightarrow C14-C15 (7.89 kcal/mol), C18-H18 \rightarrow C19-C21 (7.88 kcal/mol), C9-H9 \rightarrow C7-C8 (7.77 kcal/mol), and C9-H9 \rightarrow C8-H8 (5.15 kcal/mol). For the dimer, NBO calculations revealed $\text{LP} \rightarrow \sigma^*$ hyperconjugative intermolecular interactions in order of 4 kcal/mol between the OH groups that form the O-H-O hydrogen bonds.

3.6. Molecular Docking Studies. PASS (prediction of activity spectra) [48] is a very useful online tool that estimates the pharmacological activities of a molecule based on SAR (structure activity relationship) analysis from MDDR database (produced by Accelrys and Prous Science) [49, 50]. It works on the principle that the biological activity of a compound equates to its structure, thus comparing the molecular structure with more than 200,000 active compounds, allowing to estimate more than 3000 kinds of biological activities. The PASS prediction gives Pa (probable activity) and Pi (probable inactivity) values, which can vary from 0.000 to 1.000; in general, $\text{Pa} + \text{Pi} \neq 1$, since these probabilities are calculated independently [50]. The PASS prediction results for the studied molecule are listed in Table 3.

Among the various predicted properties, the following activities deserve attention: antioxidant, free radical scavenger, antiprotozoal, antieczematic, hypolipemic, antineoplastic,

TABLE 2: Experimental and calculated wavenumbers (cm^{-1}) and assignments for 4NRC.

IR solid	B3LYP 6-311G (2d,p)			Assignment (PED > 5%)
	Unscaled	Scaled	Intensity	
—	3844.18	3767.29	80.02	STRE O-H (100%)
	3788.51	3712.40	104.12	STRE O-H (100%)
3468	3669.00 (dimer)	3595.62 (dimer)	45.06	STRE O-H (100%)
—	3216.56	3152.23	14.82	STRE C9-H (40%) + STRE C9-H (58%)
—	3210.00	3145.80	2.60	STRE C5-H5 (99%)
—	3191.25	3127.43	6.92	STRE C1-H1 (97%)
—	3144.75	3081.86	19.99	STRE C2-H2 (97%)
—	3138.81	3076.03	16.66	STRE C9-H (43%) + STRE C9-H (36%) + STRE C8-H8 (19%)
—	3123.56	3061.09	26.65	STRE C9-H9 (12%) + STRE C8-H8 (52%) + STRE C15-H15 (22%)
—	3120.72	3058.31	34.46	STRE C8-H8 (22%) + STRE C15-H15 (66%)
—	3119.16	3056.78	37.04	STRE C20-H20 (88%)
—	3106.63	3044.50	43.06	STRE C10-H10 (36%) + STRE C10-H10 (49%)
—	3104.07	3041.99	44.93	STRE C13-H13 (42%) + STRE C18-H18 (28%)
3039	3103.64	3041.57	24.87	STRE C13-H13 (28%) + STRE C18-H18 (47%) + STRE C21-H21 (10%)
—	3097.14	3035.20	24.09	STRE C10-H10 (32%) + STRE C10-H10 (24%) + STRE C10-H10 (43%)
—	3094.65	3032.76	6.32	STRE C18-H18 (15%) + STRE C21-H21 (72%)
—	3086.36	3024.63	9.38	STRE C11-H11 (16%) + STRE C12-H12 (52%) + STRE C13-H13 (18%)
—	3076.22	3014.70	16.63	STRE C16-H16 (13%) + STRE C17-H17 (66%)
—	3069.52	3008.13	11.40	STRE C11-H11 (68%) + STRE C12-H12 (22%)
—	3056.82	2995.68	14.67	STRE C16-H16 (75%) + STRE C17-H17 (18%)
—	3052.61	2991.56	24.33	STRE C15-H15 (40%) + STRE C15-H15 (58%)
—	3045.06	2984.16	37.35	STRE C20-H20 (47%) + STRE C20-H20 (41%)
—	3041.07	2980.25	10.33	STRE C21-H21 (45%) + STRE C21-H21 (43%)
2968	3032.04	2971.40	21.51	STRE C10-H10 (24%) + STRE C10-H10 (17%) + STRE C10-H10 (55%)
—	3021.87	2961.43	24.02	STRE C11-H11 (79%) + STRE C12-H12 (10%)
—	3015.62	2957.34	36.05	STRE C12-H12 (14%) + STRE C15-H15 (42%) + STRE C15-H15 (25%)
—	3015.83	2955.51	18.95	STRE C12-H12 (67%)
—	3011.19	2950.78	49.51	STRE C20-H20 (33%) + STRE C20-H20 (39%)
—	3008.64	2948.47	26.44	STRE C17-H17 (75%)
2932	3003.19	2943.13	31.43	STRE C21-H21 (11%) + STRE C21-H21 (36%) + STRE C21-H21 (39%)
2923	2994.39	2934.50	25.08	STRE C16-H16 (90%)
—	1732.01	1697.37	2.09	STRE C19=C18 (69%)
—	1721.85	1687.41	1.30	STRE C14=C13 (70%)
—	1695.53	1661.62	10.97	STRE C9=C8 (70%) + BEND H9-C9=C8 (15%)
1636	1661.36	1628.13	17.34	STRE C1=C2 (25%) + STRE C5=C4 (12%) + STRE C3=C4 (15%)
—	1642.46	1609.61	137.8	STRE C2=C3 (10%) + STRE C6-C5 (18%) + STRE C3-C4 (25%)
1520	1550.44	1519.43	410.6	STRE C2=C3 (14%) + BEND H5-C5=C4 (14%) + BEND H1-C1-C2 (16%) + BEND H2-C2=C3 (19%)
—	1515.26	1484.95	11.49	BEND H10-C10-H10 (16%) + BEND H10-C10-H10 (50%) TORS H10-C10-C7-C11 (12%)
—	1507.78	1477.62	5.13	BEND H12-C12-H12 (42%) + BEND H15-C15-H15 (13%) + BEND H15-C15-H15 (11%)
—	1504.06	1473.98	5.53	BEND H17-C17-H17 (36%) + BEND H20-C20-H20 (12%) + BEND H20-C20-H20 (10%)
—	150281	1472.75	6.67	BEND H10-C10-H10 (18%) + BEND H10-C10-H10 (36%) + TORS H10-C10-C7-C11 (10%)
—	1498.03	1468.07	8.05	BEND H16-C16-H16 (14%) + BEND H21-C21-H21 (11%) + BEND H21-C21-H21 (10%) + BEND H21-C21-H21 (27%)
—	1495.86	1465.94	1.41	STRE C1-C2 (11%) + STRE C5=C4 (13%) + STRE C6-C5 (11%) + BEND H2-O2-C4 (17%)
—	1493.42	1463.55	10.88	BEND H21-C21-H21 (12%) + BEND H21-C21-H21 (16%) + BEND H20-C20-H20 (20%) + BEND H20-C20-H20 (27%)
—	1492.33	1462.48	7.18	BEND H16-C16-H16 (18%) BEND H15-C15-H15 (15%) + BEND H15-C15-H15 (14%)
—	1491.00	1461.18	0.40	BEND H11-C11-H11 (22%) + BEND H15-C15-H15 (24%) + BEND H15-C15-H15 (22%)
—	1485.45	1455.74	3.37	BEND H15-C15-H15 (11%) + BEND H15-C15-H15 (18%) + BEND H20-C20-H20 (16%)
—	1479.44	1449.85	1.02	BEND H11-C11-H11 (42%) + BEND H12-C12-H12 (22%)
—	1476.87	1447.33	1.42	BEND H16-C16-H16 (23%) + BEND H17-C17-H17 (20%) + BEND H15-C15-H15 (13%)
1440	1473.92	1444.44	0.38	BEND H21-C21-H21 (24%) + BEND H21-C21-H21 (22%) + BEND H20-C20-H20 (12%) + BEND H20-C20-H20 (17%)
—	1451.04	1422.02	6.48	BEND H9-C9=C8 (66%) + BEND H8-C8=C9 (13%)
1383	1423.65	1395.18	2.50	BEND H21-C21-H21 (15%) + BEND H20-C20-H20 (26%) + BEND H20-C20-H20 (12%) + BEND H20-C20-H20 (14%)

TABLE 2: Continued.

IR solid	B3LYP 6-311G (2d,p)			Assignment (PED > 5%)
	Unscaled	Scaled	Intensity	
—	1422.48	1394.03	7.08	BEND H13-C13=C14 (16%) + BEND H15-C15-H15 (15%) + BEND H15-C15-H15 (14%) + BEND H15-C15-H15 (30%)
—	1413.00	1384.74	7.77	BEND H21-C21-H21 (18%) + BEND H21-C21-H21 (18%) + BEND H21-C21-H21 (22%) + BEND H20-C20-H20 (10%)
—	1409.94	1381.74	13.36	BEND H10-C10-H10 (34%) + BEND H10-C10-H10 (25%) + BEND H10-C10-H10 (28%)
—	1398.28	1370.31	5.66	BEND H13-C13=C14 (34%) + TORS H12-C12-C13=C14 (10%)
—	1389.12	1361.34	12.91	BEND H18-C18=C19 (51%)
—	1380.32	1352.71	27.18	BEND H13-C13=C14 (10%) + TORS H11-C11-C7-C10 (15%) + TORS H11-C11-C7-C10 (22%)
—	1365.88	1338.56	2.20	STRE C2=C3 (16%) + STRE C6-C5 (11%) + BEND H1-O1-C3 (15%)
—	1362.22	1334.98	78.19	TORS H16-C16-C14-C15 (12%) + TORS H16-C16-C14-C15 (20%) + TORS H17-C16-C14-C15 (10%) + TORS H17-C16-C14-C15 (13%)
—	1356.45	1329.32	74.98	BEND H2-O2-C4 (26%) + BEND H5-C5=C4 (16%)
—	1350.93	1323.91	27.80	STRE C9=C8 (10%) + BEND H8-C8=C9 (52%)
—	1340.38	1313.57	6.17	BEND H11-C11-C7 (27%) + TORS H11-C11-C7-C10 (18%) + TORS H12-C12-C13=C14 (10%)
—	1318.91	1292.53	74.98	BEND H16-C16-C17 (12%)
—	1314.28	1287.99	72.91	BEND H16-C16-C17 (16%) BEND H17-C17-C18 (11%) + TORS H16-C16-C14-C15 (11%) + TORS H17-C16-C14-C15 (11%)
1283	1304.29	1278.20	82.73	STRE C2-C4 (10%) + BEND H2-C2=C3 (11%) + TORS H12-C12-C13=C14 (11%)
—	1287.77	1262.01	1.29	TORS H16-C16-C14-C15 (15%) + TORS H17-C16-C14-C15 (19%) + TORS H17-C16-C14-C15 (16%)
—	1281.02	1255.40	128.66	STRE O1-C3 (12%) + BEND H1-C1=C2 (11%) + BEND C2=C3-C4 (10%)
—	1263.23	1237.97	1.68	BEND H11-C11-C7 (17%) + BEND H12-C12-C13 (36%)
—	1246.74	1221.81	2.01	STRE C21-C19 (13%) + BEND H16-C16-C17 (15%) + BEND H17-C17-C18 (14%)
—	1230.92	1206.30	34.65	BEND H5-C5=C4 (12%)
—	1224.37	1199.88	37.12	STRE C5=C4 (17%) + BEND H2-O2-C4 (24%) + BEND H5-C5=C4 (15%)
—	1179.69	1156.10	54.92	STRE C1-C2 (13%) + BEND H1-O1-C3 (29%) + BEND H1-C1-C2 (12%) + BEND H2-C2=C3 (24%)
—	1175.50	1151.99	11.90	BEND H16-C16-C17 (12%) + BEND H17-C17-C18 (13%)
—	1155.11	1132.01	26.97	STRE C11-C7 (15%) + TORS H10-C10-C7-C11 (16%) + TORS H10-C10-C7-C11 (12%)
1114	1131.48	1108.85	16.00	STRE C18-C17 (31%)
—	1119.43	1097.04	58.96	BEND C1-C2=C3 (11%)
—	1106.47	1084.34	0.21	TORS H21-C21-C19-C20 (12%) + TORS H21-C21-C19-C20 (12%) + TORS H20-C20-C18=C19 (12%) + OUT C20-C21-C18=C19 (10%)
—	1103.02	1080.96	6.37	STRE C13-C12 (12%)
1082	1070.28	1048.87	3.31	BEND H15-C15-H15 (10%) + TORS H15-C15-C14-C16 (16%) + TORS H15-C15-C14-C16 (22%) + OUT C15-C16-C13=C14 (10%)
—	1062.08	1040.84	5.06	BEND H9-C9=C8 (41%) + TORS H10-C10-C7-C11 (11%) + TORS H10-C10-C7-C11 (13%)
—	1046.53	1025.60	6.05	TORS H8-C8-C7-C11 (36%)
—	1041.75	1020.92	6.73	TORS H8-C8-C7-C11 (29%)
1031	1029.04	1008.46	3.87	STRE C7-C6 (38%)
1001	1021.14	1000.72	2.40	STRE C7-C6 (12%) + TORS H18-C18=C19-C21 (16%) + TORS H21-C21-C19-C20 (14%) + TORS H20-C20-C19-C21 (16%)
—	1017.63	997.28	0.48	STRE C7-C6 (16%)
—	1004.20	984.12	1.69	STRE C17-C18 (58%)
—	966.79	947.45	4.51	STRE C10-C7 (14%) + BEND H11-C11-C7 (10%)
—	962.14	942.90	0.30	STRE C20-C19 (15%) + TORS H21-C21-C19-C20 (16%) + TORS H21-C21-C19-C20 (13%) + TORS H20-C20-C18=C19 (12%) + TORS H20-C20-C19-C21 (10%)
—	953.82	934.74	27.99	TORS H9-C9=C8-C7 (36%) + TORS H9-C9=C8-C7 (60%)
—	944.03	925.15	13.30	STRE C2-C4 (10%) + BEND C1-C2=C3 (14%) + TORS H10-C10-C7-C11 (10%)
—	942.63	923.78	13.62	STRE C11-C7 (21%) + TORS H10-C10-C7-C11 (13%)
912	925.15	906.65	2.04	TORS H1-C1-C2=C3 (47%) + TORS H2-C2=C3-C4 (28%)
888	899.96	881.96	9.79	TORS H5-C5=C4-C3 (39%) + TORS H13-C13=C14-C16 (25%)
—	885.19	867.49	7.13	TORS H5-C5=C4-C3 (24%) + TORS H13-C13=C14-C16 (27%)
—	864.35	847.06	7.09	TORS H18-C18=C19-C21 (49%)
—	835.78	819.06	2.02	STRE C7-C8 (10%) + STRE C11-C7 (10%) + BEND H9-C9=C8 (11%)
810	812.60	796.35	2.02	STRE C15-C14 (11%) + STRE C21-C19 (12%) + STRE C20-C19 (24%)
—	805.80	789.68	24.74	TORS H1-C1-C2=C3 (26%) + TORS H2-C2=C3-C4 (43%)
—	802.76	786.70	10.62	STRE C15-C14 (18%) + STRE C16-C14 (10%)
783	798.09	782.13	27.94	STRE C2=C3 (11%) + STRE C3-C4 (27%) + STRE O1-C3 (16%)

TABLE 2: Continued.

IR solid	B3LYP 6-311G (2d,p)			Assignment (PED > 5%)
	Unscaled	Scaled	Intensity	
—	764.37	749.08	1.76	TORS H11-C11-C7-C10 (12%)
—	754.43	739.34	4.35	STRE C21-C19 (10%) + STRE C20-C19 (10%) + TORS H17-C16-C14-C15 (11%)
—	736.31	721.58	2.16	TORS H5-C5=C4-C3 (12%) + TORS C2=C3-C4=C5 (18%) + TORS C1-C2=C3-C4 (19%) + TORS C6-C5=C4-C3 (20%) + OUT O1-C2-C4-C3 (10%)
—	701.85	687.81	7.48	TORS H9-C9=C8-C7 (31%) + TORS H9-C9=C8-C7 (13%)
667	681.03	667.41	6.40	STRE C8-C7 (10%) + STRE C7-C6 (10%) + STRE C10-C7 (17%) + BEND C2=C3-C4 (13%)
—	661.25	648.03	13.60	OUT O2-C5-C3-C4 (25%) + OUT O1-C2-C4-C3 (11%) + OUT C7-C1-C5-C6 (11%)
—	597.40	585.45	1.69	BEND C5=C4-C3 (10%) + BEND O1-C3-C4 (11%)
593	595.97	584.05	18.75	BEND C5=C4-C3 (10%) + BEND O1-C3-C4 (18%)
—	544.30	533.41	4.65	BEND C19=C18-C17 (12%) + BEND C21-C19=C18 (10%)
—	507.18	497.04	3.35	BEND C2=C3-C4 (12%) + BEND O2-C4=C5 (10%)

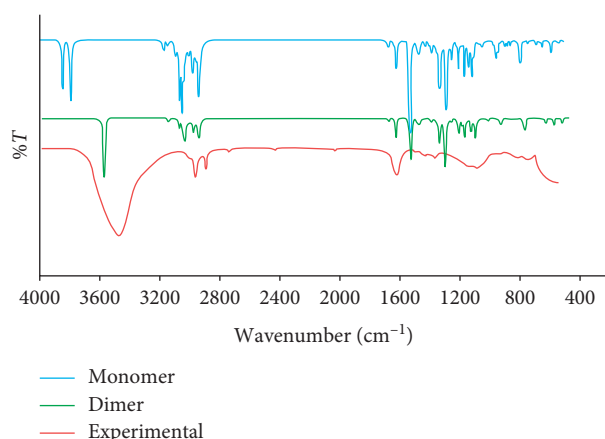


FIGURE 6: Comparison between experimental and calculated spectra of 4NRC.

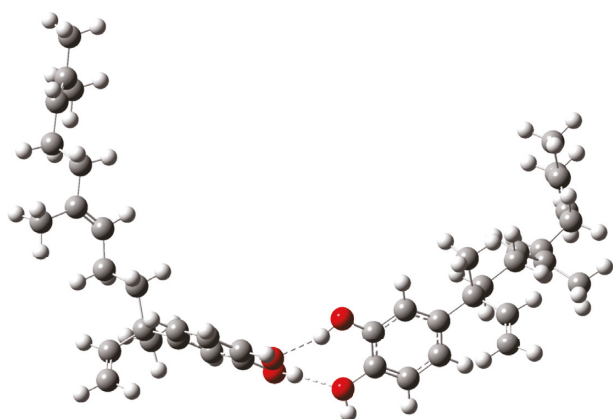


FIGURE 7: Proposed dimer for 4NRC.

hepatoprotectant, antihelminthic, lipid metabolism regulator, cholesterol inhibitor, MMP9 expression inhibitor, and topoisomerase I inhibitor. In fact, some of these activities have been confirmed in vitro [9, 11–13, 15–18, 20]. Guided by the antineoplastic activity of 4NRC, molecular docking calculations were performed on AutoDock-Vina [51] with DNA Topoisomerase I complex with DNA (topo I-DNA) due to the fact that a large number of structures used for the

treatment of human (antineoplastic) cancers, such as brain, ovary, colon, and lung cancers are eukaryotic topo I inhibitors. The second enzyme chosen for docking calculations was *Plasmodium falciparum* lactate dehydrogenase (PfLDH) due to the parasite's dependence on glycolysis for energy production. Because the lactate dehydrogenase (LDH) enzymes found in *P. vivax*, *P. malariae*, and *P. ovale* (pLDH) exhibit great similarity to PfLDH (about 90%), this enzyme is an effective drug target against malaria [52]. Human glyceraldehyde 3-phosphate dehydrogenase (GAPDH) was the third target enzyme chosen because it catalyzes the sixth step of glycolysis and thus serves to break down glucose for energy and carbon molecules. The glycolytic and anti-apoptotic functions of this enzyme promote tumorigenesis because they contribute to the proliferation and protection of tumor cells. GAPDH is overexpressed in multiple human cancers, such as cutaneous melanoma, being positively correlated with tumor progression [53, 54].

The docking calculations in AutoDock Vina (ADTV) consist in a number of sequential steps, where each step involves a random perturbation of the conformation followed by a local optimization that uses the Broyden-Fletcher-Goldfarb-Shanno algorithm [55] (an efficient quasi-Newton method). Each local optimization involves many “evaluations” of the scoring function as well as its derivatives in the position-orientation-torsion coordinates, resulting in structures that are accepted or not [51, 55]. The X-ray crystal structure of human topoisomerase I (PDB ID: 1k4t) [56], *Plasmodium falciparum* lactate dehydrogenase (PDB ID: 1cet) [57], and GAPDH (PDB ID: 1u8F) [58] were obtained from the Protein Data Bank website (<http://www.rcsb.org/pdb/>). For topoisomerase I, water molecules and topotecan were removed; Gasteiger charges were assigned to the PDBQT file format generated by ADTV. A grid box size of $10 \times 16 \times 10 \text{ \AA}$ was centered at the site of DNA cleavage of topo I-DNA complex ($x = 21.260$, $y = -3.683$, and $z = 28.289$). For *Plasmodium falciparum* lactate dehydrogenase, a grid box size of $16 \times 16 \times 10 \text{ \AA}$ was centered at the site of chloroquine interaction ($x = 35.726$, $y = 10.811$, and $z = 19.711$). For GAPDH, the same procedure was performed with a grid box size of $18 \times 20 \times 20 \text{ \AA}$ centered at the site of NAD interaction (Figure S1(c)). The validation of each grid box was done by removing the ligands (inhibitor) and

TABLE 3: PASS prediction for the activity spectrum of 4NRC with Pa > 0.4

Pa	Pi	Activity name
0.959	0.003	Mucomembranous protector
0.865	0.002	Undecaprenyl phosphate mannosyltransferase inhibitor
0.847	0.003	Prenyl-diphosphatase inhibitor
0.858	0.018	Aspulvinone dimethylallyltransferase inhibitor
0.819	0.003	Antioxidant
0.819	0.005	UDP-glucuronosyltransferase inhibitor
0.782	0.005	Fatty-acyl-CoA synthase inhibitor
0.768	0.004	Beta-carotene 15,15-monooxygenase inhibitor
0.774	0.015	Beta-adrenergic receptor kinase inhibitor
0.774	0.015	G-protein-coupled receptor kinase inhibitor
0.748	0.002	Retinol dehydrogenase inhibitor
0.783	0.038	Ubiquinol-cytochrome-c reductase inhibitor
0.746	0.038	Steroid N-acetylglucosaminyltransferase inhibitor
0.742	0.003	Plastoquinol-plastocyanin reductase inhibitor
0.748	0.008	Lipid metabolism regulator
0.740	0.004	Free radical scavenger
0.740	0.033	Antieczematic
0.710	0.007	Hypolipemic
0.708	0.025	Antioneoplastic
0.690	0.003	Antiviral (rhinovirus)
0.599	0.023	Gastrin inhibitor
0.588	0.013	Hepatoprotectant
0.589	0.015	Antiprotozoal
0.575	0.006	Dolichyl-phosphatase inhibitor
0.573	0.023	Cholesterol antagonist
0.552	0.006	Membrane permeability enhancer
0.563	0.019	Radioprotector
0.564	0.021	Antisecretoric
0.471	0.007	Hemostatic
0.491	0.028	Leukotriene-B4 20-monooxygenase inhibitor
0.504	0.045	Feruloyl esterase inhibitor
0.564	0.021	Antisecretoric
0.525	0.027	Antifungal
0.497	0.024	Antipsoriatic
0.553	0.011	Antiparasitic
0.504	0.018	Carminative
0.462	0.009	Antihelmintic
0.571	0.038	Anti-inflammatory
0.564	0.021	Antisecretoric
0.488	0.031	CYP3A3 substrate
0.462	0.009	Antihelmintic
0.474	0.022	Antineoplastic (breast cancer)
0.467	0.017	Antimutagenic
0.453	0.017	Topoisomerase I inhibitor
0.447	0.042	Lactase inhibitor
0.452	0.004	Neurotrophic factor enhancer
0.679	0.008	MMP9 expression inhibitor

redocking them at the same site using the proposed grid box. Then, a comparison between the docked structure and the X-ray structure was performed through the RMSD calculation. For all the performed calculations, the obtained RMSD values were lower than 2 (Figures S1(a)–S1(c)).

Free energy of binding (ΔG) analysis demonstrated that 4NRC molecule docked with ΔG values of -6.3 , -6.5 , and -7.6 kcal/mol with PflLDH, TOPO I, and GAPDH, respectively, while the known inhibitors (or ligands) docked

with ΔG values of -7.0 , -12.6 , and -10.6 kcal/mol, respectively (Figure 8). Binding modes analysis demonstrated that the title molecule docked at the PflLDH site similar to chloroquine (Figure 8(a)); however, studies confirm that chloroquine acts as a weak inhibitor of PflLDH, with mild selectivity for the parasite enzyme [56], but low levels of inhibition may contribute to the biological efficacy of the drug, a factor that seems to apply to 4NRC molecule too. 4NRC binds at the site of the macromolecule by noncovalent alkyl-alkyl and alkyl- π interactions, where the catechol moiety interacts with Ala 98 and Ile54 (alkyl- π) and the side chain interacts with Phe 100, Ile 119, Leu 115, and Lys 118 residues (alkyl-alkyl, Figure 9(a)). A hydrogen bond between the hydroxyl group of the catechol moiety and Tyr 85 residue was also confirmed.

With TOPO I, the binding modes analysis showed that 4NRC docked at the site of DNA cleavage, between the base pairing, similar to topotecan (Figure 8(b)); however, for having four conjugated aromatic rings and a planar structure, topotecan molecule presents a lower ΔG and a more effective docking than 4NRC. On the other hand, the calculations for 4NRC revealed that catechol moiety binds to DC 112, DA 113, and TGP11 base pairs by π - π interactions, besides forming a hydrogen bond (with the DC 112 base). The side chain interacts by weak noncovalent interaction with Glu 356, preventing the DNA cleavage (see Figure 9(b)). For GAPDH, the binding modes revealed that 4NRC binds at the site similar to NAD molecule (Figure 8(c)). Despite the high value of ΔG in relation to ligand, the catechol moiety of 4NRC forms an intermolecular hydrogen bond with ASN9, which makes 4NRC a competitive inhibitor for this essential glycolytic enzyme. Weak π -alkyl and alkyl-alkyl type interactions with Asp35, Gly10, Thr99, Ile14, and Arg13 residues were also registered in the active site, thus contributing to the inhibition of GAPDH (Figure 9(c)).

4. Conclusion

4-Nerolidylcatechol was comprehensively characterized with its spectral behavior and quantum properties described. The interatomic distances and angles proved to be plausible compared to the X-ray data for a similar structure. The conformational analysis of 4NRC showed seven stable conformations in the gas phase, but, comparing the potential energies values, conformer B is the most stable rotamer by an average $\Delta E \approx 0.1$ kcal/mol. The small HOMO-LUMO energy gap calculated for both structures are directly related to their amount of chemical hardness (2.83 eV), which lead to classifying them as soft molecules when compared to other structures in the associated literature. The electronegativity (χ) and electrophilicity index (ω) values reveal that 4NRC has good attractive power and acts as a moderate electrophile, which can justify in part its known antioxidant potential. The comparative IR studies showed that the intermolecular hydrogen bonds of the proposed dimer are plausible (making them closest to the experimental ones) and also revealed several characteristic vibrations of 4NRC, thus complementing the vibrational study for these type of

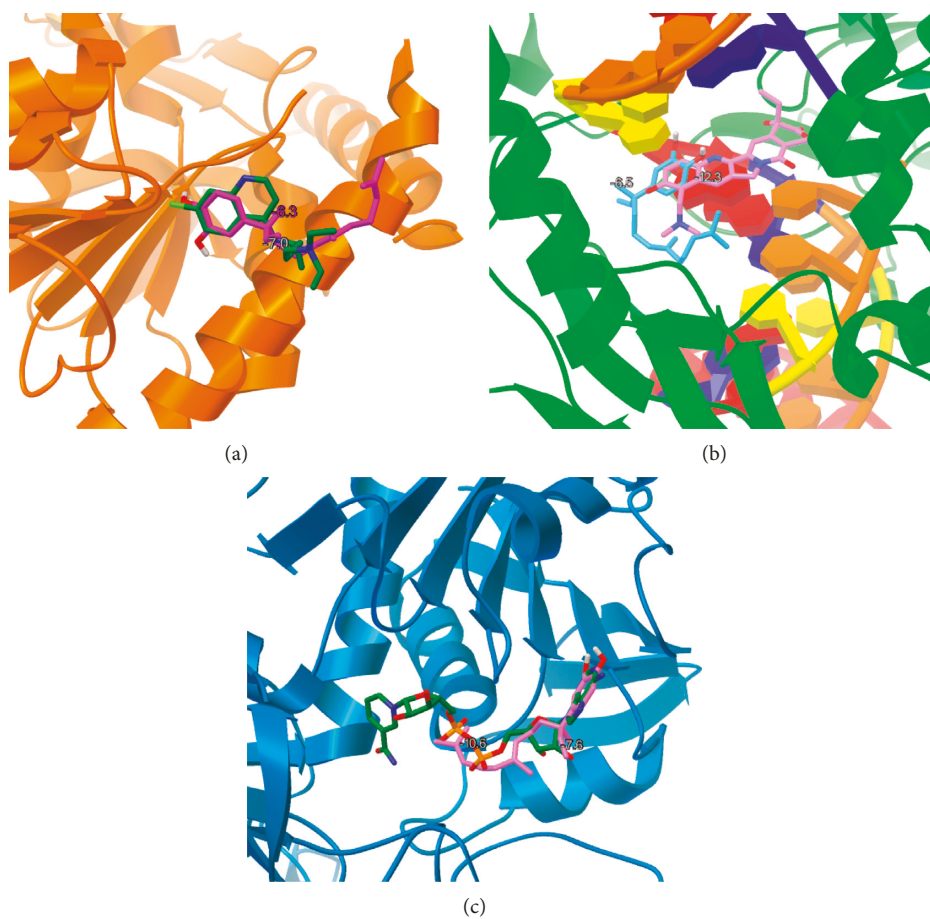


FIGURE 8: Superimpositions of the docked 4NRC structures and cocrystallized ligands into the selected enzymes, PflDH, TOPO I, and GAPDH. (a) Comparison of the docked 4NRC (magenta) and cocrystallized structure of chloroquine (green); (b) comparison of the docked 4NRC (blue) and cocrystallized structure of topotecan (pink); (c) comparison of the docked 4NRC (pink) and cocrystallized structure of NADH (green).

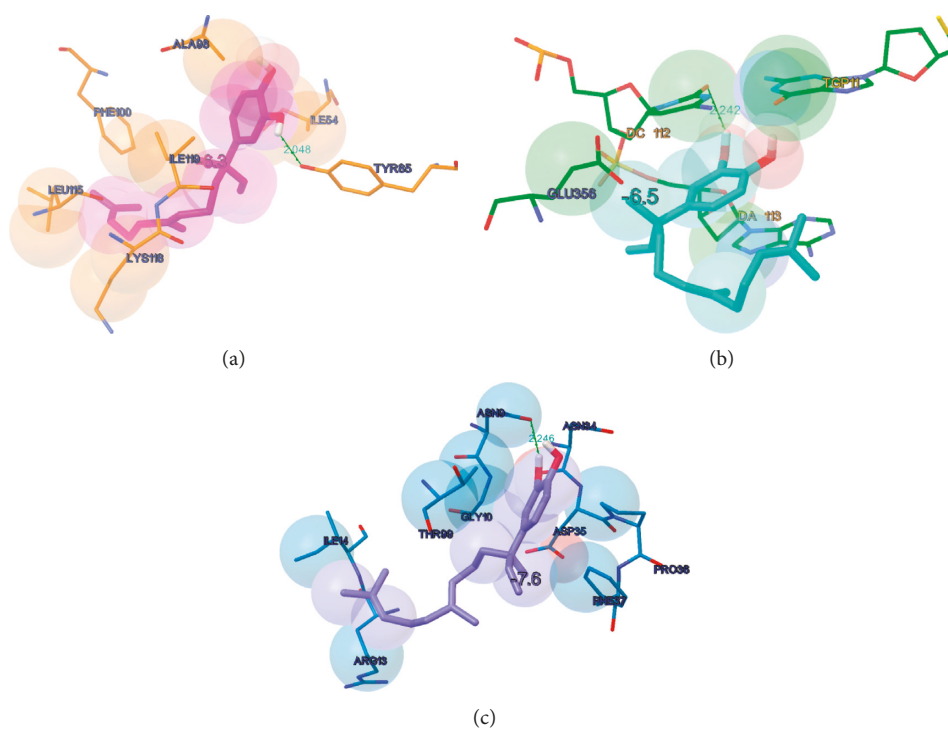


FIGURE 9: Binding modes of the 4NRC docked to PflDH (a), TOPO I (b), and GAPDH (c). Green lines indicate hydrogen bonds.

molecules. The molecular docking results revealed good interactions of the title molecule with the DNA-topoisomerase I complex, glyceraldehyde 3-phosphate dehydrogenase (GAPDH), and *Plasmodium falciparum* lactate dehydrogenase (PfLDH), critical enzymes for antimalarial and antitumor activities.

Data Availability

The data used to support the findings of this study are included within the article.

Conflicts of Interest

The authors declare that there are no conflicts of interest regarding the publication of this paper.

Acknowledgments

The authors thank FINEP, CAPES, FAPEAM, and CNPq for the financial support and the NANOPOL Laboratory, LABIV (Infra red Laboratory), and NMRLAB (NMR laboratory) of the Analytical Center of Federal University of Amazonas for the spectra obtained.

Supplementary Materials

Table S1: calculated geometrical parameters for 4NRC. Table S2: selected second-order perturbation energies of 4NRC. Figure S1: validation of the docking calculations: (a) superimposition of the docked (pink) and cocrystallized (dark blue) structures of topotecan into the DNA cleavage site of DNA topoisomerase I; (b) superimposition of the docked (magenta) and cocrystallized (green) structures of chloroquine into the active site of *Plasmodium falciparum* lactate dehydrogenase; (c) superimposition of the docked (magenta) and cocrystallized (green) structures of NAD into the active site of GAPDH enzyme. (*Supplementary Materials*)

References

- [1] Q. Wu, D. Yan, Y. Chen et al., "A redox-neutral catechol synthesis," *Nature Communications*, vol. 8, article 14227, 2017.
- [2] S. Mogwitz, J. Buse, S. Ehrlich, and V. Roessner, "Clinical pharmacology of dopamine-modulating agents in Tourette's syndrome," *International Review of Neurobiology*, vol. 112, pp. 281–349, 2013.
- [3] H. Fiege, H. W. Voges, T. Hamamoto et al., "Phenol derivatives," *Ullmann's Encyclopedia of Industrial Chemistry*, John Wiley & Sons, Hoboken, NJ, USA, 6th edition, 2000.
- [4] F. Emilie, F. D. Céline, J. Christine et al., "Catechols as versatile platforms in polymer chemistry," *Progress in Polymer Science*, vol. 38, pp. 236–270, 2013.
- [5] N. Schweigert, A. J. B. Zehnder, and R. I. L. Eggen, "Chemical properties of catechols and their molecular modes of toxic action in cells, from microorganisms to mammals. Minireview," *Environmental Microbiology*, vol. 3, no. 2, pp. 81–91, 2001.
- [6] J. W. Porteus and R. T. Williams, "Studies in detoxication. 20. The metabolism of benzene. II. The isolation of phenol, catechol, quinol and hydroxyquinol from the ethereal sulphate fraction of the urine of rabbits receiving benzene orally," *Biochemical Journal*, vol. 44, no. 1, pp. 56–61, 1948.
- [7] J. Yang, M. A. Cohen Stuart, and M. Kamperman, "Jack of all trades: versatile catechol crosslinking mechanisms," *Chemical Society Reviews*, vol. 43, no. 24, pp. 8271–8298, 2014.
- [8] C. D. Ropke, T. C. H. Sawada, V. V. da Silva, N. S. Michalany, and S. B. de Moraes Barros, "Photoprotective effect of *Pothomorphe umbellata* root extract against ultraviolet radiation induced chronic skin damage in the hairless mouse," *Clinical and Experimental Dermatology*, vol. 30, no. 3, pp. 272–276, 2005.
- [9] C. R. M. Da Cunha, S. A. M. Neto, C. C. Da Silva et al., "4-Nerolidylcatechol and its synthetic analogues: Antioxidant activity and toxicity evaluation," *European Journal of Medicinal Chemistry*, vol. 62, pp. 371–378, 2013.
- [10] A. Kijjoa, A. Giesbrecht, M. Akisue, O. Gottlieb, and H. Gottlieb, "4-Nerolidylcatechol from *Pothomorphe umbellata*," *Planta Medica*, vol. 39, no. 5, pp. 85–87, 2008.
- [11] E. S. Lima, A. C. S. Pinto, K. L. Nogueira et al., "Stability and Antioxidant Activity of Semi-synthetic Derivatives of 4-Nerolidylcatechol," *Molecules*, vol. 18, no. 1, pp. 178–189, 2013.
- [12] A. P. Lopes, B. S. Bagatela, P. C. P. Rosa et al., "Antioxidant and cytotoxic effects of crude extract, fractions and 4-nerolidylcatechol from aerial parts of *Pothomorphe umbellata* L. (Piperaceae)," *BioMed Research International*, vol. 2013, Article ID 206581, 5 pages, 2013.
- [13] E. Mongelli, F. Desmarchelier, J. Coussio, and G. Ciccía, "Antimicrobial activity and interaction with DNA of medicinal plants from the Peruvian Amazon region," *Revista Argentina de Microbiología*, vol. 27, pp. 199–203, 1995.
- [14] F. F. Perazzo, G. H. B. Souza, W. Lopes et al., "Anti-inflammatory and analgesic properties of water-ethanolic extract from *Pothomorphe umbellata* (Piperaceae) aerial parts," *Journal of Ethnopharmacology*, vol. 99, no. 2, pp. 215–220, 2005.
- [15] C. A. Brohem, T. C. H. Sawada, R. R. Massaro et al., "Apoptosis induction by 4-nerolidylcatechol in melanoma cell lines," *Toxicology in Vitro*, vol. 23, no. 1, pp. 111–119, 2009.
- [16] E. Mongelli, A. Romano, C. Desmarchelier, J. Coussio, and G. Ciccía, "Cytotoxic 4-nerolidylcatechol from *Pothomorphe peltata* inhibits topoisomerase I activity," *Planta Medica*, vol. 65, no. 4, pp. 376–378, 2007.
- [17] L. F. R. Silva, K. L. Nogueira, A. C. S. Pinto et al., "In vivo antimalarial activity and mechanisms of action of 4-nerolidylcatechol derivatives," *Antimicrobial Agents and Chemotherapy*, vol. 59, no. 6, pp. 3271–3380, 2015.
- [18] A. Pinto, F. Chaves, P. dos Santos, C. Nunez, W. Tadei, and A. Pohlit, "*Piper peltatum*: biomass and 4-nerolidylcatechol production," *Planta Medica*, vol. 76, no. 13, pp. 1473–1476, 2010.
- [19] K. R. Rezende and S. B. d. M. Barros, "Quantification of 4-nerolidylcatechol from *Pothomorphe umbellata* (Piperaceae) in rat plasma samples by HPLC-UV," *Revista Brasileira de Ciências Farmacêuticas*, vol. 40, no. 3, pp. 373–380, 2004.
- [20] K. S. Fernandes, A. H. M. Silva, S. A. Mendanha, K. R. Rezende, and A. Alonso, "Antioxidant effect of 4-nerolidylcatechol and α -tocopherol in erythrocyte ghost membranes and phospholipid bilayers," *Brazilian Journal of Medical and Biological Research*, vol. 46, no. 9, pp. 780–788, 2013.
- [21] E. A. Costa, R. C. Lino, M. N. Gomes et al., "Anti-inflammatory and antinociceptive activities of LQFM002—a 4-nerolidylcatechol derivative," *Life Sciences*, vol. 92, no. 3, pp. 237–244, 2013.

- [22] K. R. Gustafson, J. H. Cardellina, J. B. McMahon, L. K. Pannell, G. M. Cragg, and M. R. Boyd, "HIV inhibitory natural products. 6. The peltatols, novel HIV-inhibitory catechol derivatives from *Pothomorphe peltata*," *Journal of Organic Chemistry*, vol. 57, no. 10, pp. 2809–2811, 1992.
- [23] R. A. Costa, K. M. T. Oliveira, E. V. Costa, and M. L. B. Pinheiro, "Vibrational, structural and electronic properties investigation by DFT calculations and molecular docking studies with DNA topoisomerase II of strychnobrasiline type alkaloids: a theoretical approach for potentially bioactive molecules," *Journal of Molecular Structure*, vol. 1145, pp. 254–267, 2017.
- [24] R. A. Costa, E. A. S. Junior, G. B. P. Lopes et al., "Structural, vibrational, UV-vis, quantum-chemical properties, molecular docking and anti-cancer activity study of annomontine and N-hydroxyannomontine β -carboline alkaloids: A combined experimental and DFT approach," *Journal of Molecular Structure*, vol. 1171, no. 5, pp. 682–695, 2018.
- [25] R. A. Costa, K. M. T. Oliveira, R. de Cássia Saraiva Nunomura et al., "Quantum chemical properties investigation and molecular docking analysis with DNA topoisomerase II of β -carboline indole alkaloids from *Simaba guianensis*: a combined experimental and theoretical DFT study," *Structural Chemistry*, vol. 29, no. 1, pp. 299–314, 2017.
- [26] R. A. Costa, M. L. B. Pinheiro, K. M. T. Oliveira et al., "Structural, vibrational, and electronic properties of the glucoalkaloid strictosidine: a combined experimental and theoretical study," *Journal of Chemistry*, vol. 2016, Article ID 1752429, 16 pages, 2016.
- [27] L. A. Soares, A. F. V. B. Leal, L. F. Fraceto et al., "Host-guest system of 4-nerolidylcatechol in 2-hydroxypropyl- β -cyclodextrin: preparation, characterization and molecular modeling," *Journal of Inclusion Phenomena and Macrocyclic Chemistry*, vol. 64, no. 1-2, pp. 23–35, 2009.
- [28] M. J. Frisch, G. W. Trucks, H. B. Schlegel et al., *Gaussian 09*, Gaussian, Inc., Wallingford, UK, 2009.
- [29] R. Dennington, T. Keith, and J. Millam, *Gaussian Version 5*, Semichem Inc., Shawnee Missions KS, USA, 2009.
- [30] M. Jamroz, *Vibrational Energy Distribution Analysis, VEDA 4 Computer Program*, Poland, 2004.
- [31] S. F. Boys and F. Bernardi, "The calculation of small molecular interactions by the differences of separate total energies. Some procedures with reduced errors," *Molecular Physics*, vol. 19, no. 4, pp. 553–566, 2006.
- [32] J. Geiseke, "The structure of the catecholamines. V. The crystal and molecular structure of epinine hydrobromide," *Acta Crystallographica Section B Structural Crystallography and Crystal Chemistry*, vol. 32, no. 8, pp. 2337–2340, 1976.
- [33] R. G. Parr and R. G. Pearson, "Absolute hardness: companion parameter to absolute electronegativity," *Journal of the American Chemical Society*, vol. 105, no. 26, pp. 7512–7516, 1983.
- [34] R. Parr and W. Yang, *Functional Theory of Atoms and Molecules*, Oxford University Press, New York, NY, USA, 1989.
- [35] G. Zhang and C. B. Musgrave, "Comparison of DFT methods for molecular orbital eigenvalue calculations," *Journal of Physical Chemistry A*, vol. 111, no. 8, pp. 1554–1561, 2007.
- [36] J. F. Janak, "Proof that $\partial E/\partial n_i = \epsilon_i$ density-functional theory," *Physical Review B*, vol. 18, no. 12, pp. 7165–7168, 1978.
- [37] J. P. Perdew, R. G. Parr, M. Levy, and J. L. Balduz, "Density-functional theory for fractional particle number: derivative discontinuities of the energy," *Physical Review Letters*, vol. 49, no. 23, pp. 1691–1694, 1982.
- [38] C. G. Zhan, J. A. Nichols, and D. A. Dixon, "Ionization potential, electron affinity, electronegativity, hardness, and electron excitation energy: molecular properties from density functional theory orbital energies," *Journal of Physical Chemistry A*, vol. 107, no. 20, pp. 4184–4195, 2003.
- [39] R. G. Parr, L. V. Szentpaly, and S. Liu, "Electrophilicity index," *Journal of the American Chemical Society*, vol. 121, no. 9, pp. 1922–1924, 1999.
- [40] L. R. Domingo and P. Pérez, "The nucleophilicity N index in organic chemistry," *Organic & Biomolecular Chemistry*, vol. 9, no. 20, pp. 7168–7175, 2011.
- [41] B. C. Carlson and J. M. Keller, "Orthogonalization procedures and the localization of Wannier functions," *Physical Review*, vol. 105, no. 1, pp. 102–103, 1957.
- [42] F. Weinhold and J. E. Carpenter, "Analysis of the geometry of the hydroxymethyl radical by the "different hybrids for different spins" natural bond orbital procedure," *Journal of Molecular Structure: Theochem*, vol. 169, pp. 41–62, 1988.
- [43] A. E. Reed, R. B. Weinstock, and F. Weinhold, "Natural population analysis," *Journal of Chemical Physics*, vol. 83, no. 2, pp. 735–739, 1985.
- [44] E. R. Davidson, *Reduced Density Matrices in Quantum Chemistry*, Academic Press, New York, NY, USA, 1976.
- [45] R. S. Mulliken, "Electronic population analysis on ICAO-MO molecular wave functions. I," *Journal of Chemical Physics*, vol. 23, no. 10, pp. 1833–1841, 1955.
- [46] A. E. Reed and F. Weinhold, "Natural bond orbital analysis of near-Hartree-Fock water dimer," *Journal of Chemical Physics*, vol. 78, no. 6, pp. 4066–4073, 1983.
- [47] J. K. Badenhoop and F. Weinhold, "Natural bond orbital analysis of steric interactions," *Journal of Chemical Physics*, vol. 107, no. 14, pp. 5406–5421, 1997.
- [48] A. Lagunin, A. Stepanchikova, D. Filimonov, and V. Poroikov, "PASS: prediction of activity spectra for biologically active substances," *Bioinformatics*, vol. 16, no. 8, pp. 747–748, 2000.
- [49] S. Parasuraman, "Prediction of activity spectra for substances," *Journal of Pharmacology and Pharmacotherapeutics*, vol. 2, no. 1, pp. 52–53, 2017.
- [50] R. Prameley and T. L. S. Raj, "Prediction of biological activity spectra of a few phytoconstituents of *Azadirachta indica* A. Juss.," *Journal of Biochemical Technology*, vol. 3, pp. 375–379, 2012.
- [51] O. Trott and A. J. Olson, "AutoDock vina: improving the speed and accuracy of docking with a new scoring function, efficient optimization, and multithreading," *Journal of Computational Chemistry*, vol. 31, pp. 455–461, 2010.
- [52] J. Penna-Coutinho, W. A. Cortopassi, A. A. Oliveira, T. C. França, and A. U. Krettli, "Antimalarial activity of potential inhibitors of plasmodium falciparum lactate dehydrogenase enzyme selected by docking studies," *PLoS One*, vol. 6, Article ID e21237, 2011.
- [53] D. Ramos, A. Pellín-Carcelén, J. Agustí et al., "Deregulation of glyceraldehyde-3-phosphate dehydrogenase expression during tumor progression of human cutaneous melanoma," *Anticancer Research*, vol. 35, pp. 439–444, 2015.
- [54] D. Wang, D. R. Moothart, D. R. Lowy, and X. Qian, "The expression of glyceraldehyde-3-phosphate dehydrogenase associated cell cycle (gacc) genes correlates with cancer stage and poor survival in patients with solid tumors," *PLoS One*, vol. 8, Article ID e61262, 2013.
- [55] J. Nocedal and S. J. Wright, *Numerical Optimization*, Springer Series in Operations Research, Springer-Verlag, Berlin, Germany, 1999.

- [56] B. L. Staker, K. Hjerrild, M. D. Feese, C. A. Behnke, A. B. Burgin Jr., and L. J. Stewart, "Nonlinear partial differential equations and applications: the mechanism of topoisomerase I poisoning by a camptothecin analog," *Proceedings of the National Academy of Sciences*, vol. 99, no. 24, pp. 15387–15392, 2002.
- [57] J. A. Read, K. W. Wilkinson, R. Tranter, R. B. Sessions, and R. L. Brady, "Chloroquine binds in the cofactor binding site of *Plasmodium falciparum* lactate dehydrogenase," *Journal of Biological Chemistry*, vol. 274, no. 15, pp. 10213–10218, 1999.
- [58] J. L. Jenkins and J. J. Tanner, "High-resolution structure of human D-glyceraldehyde-3-phosphate dehydrogenase," *Acta Crystallographica Section D Biological Crystallography*, vol. 62, no. 3, pp. 290–301, 2006.



Hindawi

Submit your manuscripts at
www.hindawi.com

